Nonreciprocal non-Hermitian Su-Schrieffer-Heeger chain modulated by the influence of $\mathcal{PT}$-symmetric imaginary potentials

Chen-Hao Zhao,[1] Jia-Rui Li,[1] Cui Jiang,[2] Lian-Lian Zhang,[1] and Wei-Jiang Gong[1,*]

[1]*College of Sciences, Northeastern University, Shenyang 110819, China*

[2]*Basic Department, Shenyang Institute of Engineering, Shenyang 110136, China*

(Received 25 November 2023; accepted 22 March 2024; published 8 April 2024)

We concentrate on the skin effects and topological edge states in the nonreciprocal non-Hermitian Su-Schrieffer-Heeger (SSH) chain, by taking into account the presence of $\mathcal{PT}$-symmetric imaginary potentials. Following a detailed demonstration of the theoretical method, we find that, regardless of the application manner of $\mathcal{PT}$-symmetric imaginary potentials, they take weak impacts from the skin effect of bulk states, but efficiently modulate the topological edge states. On the other hand, if such potentials are applied according to two domains, the skin effect and new edge states can be induced along the domain wall, which are also dependent on the structural parameters. Therefore, the findings in this paper promote understanding of the independent modulations of the skin effects and topological edge states via the interplay between the imaginary potentials and nonreciprocal couplings in the SSH lattices.

DOI: 10.1103/PhysRevA.109.042203

I. INTRODUCTION

Non-Hermitian systems are open structures that can be described by non-Hermitian Hamiltonians. During the past years, they have attracted great interest from both theoretical and experimental perspectives [1–5]. With the development of topological systems, non-Hermitian topological systems have been found to possess profound application values in enhanced sensing [6–8], topological lasers [9], and topological optical funneling [10]. Presently, there are two ways to achieve non-Hermitian systems: using gain and loss potentials [11–14] and nonreciprocal couplings [15–17].

The most famous system of gain and loss potentials is the parity-time ($\mathcal{PT}$) symmetry system. In 1998, Bender and Boettcher first discovered that non-Hermitian Hamiltonians with $\mathcal{PT}$ symmetry can display completely real energy spectra [18]. This indeed promotes the development of researches on non-Hermitian systems [19]. On the experimental side, researchers have found that $\mathcal{PT}$-symmetric systems can be achieved in optics [20–22], topological circuits [23,24], and topological photonic structures [25–27]. Moreover, many groups prefer to introduce $\mathcal{PT}$-symmetric imaginary potentials with gain and loss into topological systems to discuss the mechanisms of new phase transition and $\mathcal{PT}$-symmetric transition, such as the one-dimensional (1D) Su-Schrieffer-Heeger (SSH) model, trimer lattices, graphene, two-dimensional SSH lattices, and the Kitaev model [28–35].

The other non-Hermitian mechanism is the nonreciprocal coupling by asymmetric intensity of the hopping amplitudes between the lattice points. According to the previous reports, this characteristic causes the systems to display the non-Hermitian skin effect (NHSE), that is, eigenstates under open boundary conditions are localized near the boundary of the system in the form of exponential decay in 1D systems [10,36–39]. Due to the occurrence of NHSE, the bulk-boundary correspondence of the system completely collapses [36,40]. During the past years, research groups discussed the topological characteristics in the nonreciprocal topological structures and proposed some concepts, such as generalized Brillouin zone (GBZ) [36,41–43], non-Bloch bulk-boundary correspondence [36], non-Bloch topological invariants [36,41], and non-Bloch electronic polarization [44,45]. Meanwhile in experiment, NHSE has been realized and applied, including the utilization of cold atoms, quantum optical systems, optical grid systems, and topolectrical circuits [46–50].

In view of the research progress about the systems with imaginary potentials or nonreciprocal couplings, it is natural to think about the interplay between these two mechanisms in the modification of skin effect and topological edge states. Motivated by such a topic, in the present paper we concentrate on the skin effects and topological edge states in the nonreciprocal non-Hermitian SSH chain, by taking into account the presence of $\mathcal{PT}$-symmetric imaginary potentials. Our purpose is to provide a way to predict the skin effect of bulk states and localization of edge states, and then provide some credible results to separate the specific edge state from bulk states and analyze the topological properties of the SSH chain. The calculation results show that the $\mathcal{PT}$-symmetric imaginary potentials take weak impact from the skin effect, but efficiently modulate the topological edge states, regardless of the application manners of them. Alternatively, if such potentials are applied according to two domains, the skin effect and new edge states can be induced along the domain wall, which are also dependent on the structural parameters. We thus believe that the findings in this paper promote understanding of the

*gwj@mail.neu.edu.cn

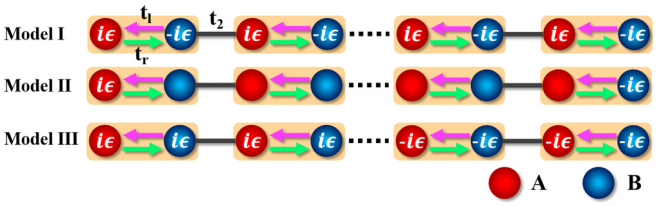

FIG. 1. Three models of our considered nonreciprocal non-Hermitian SSH chain. In case I, $\mathcal{PT}$-symmetric imaginary potentials are introduced according to the cells. In case II, the $\mathcal{PT}$-symmetric imaginary potentials are introduced to the end sites, whereas in case III such imaginary potentials are applied according to the left and right domains of the SSH chain.

independent modulations of the skin effects and topological edge states via the interplay between the imaginary potentials and nonreciprocal couplings in the SSH lattices.

II. MODEL

The nonreciprocal non-Hermitian SSH chain that we consider is illustrated in Fig. 1. It is composed of N cells and each unit cell has two distinct sites A and B, respectively. Moreover, we only consider the nearest-neighboring hopping in this chain, and then the whole system can be described by the following Hamiltonian:

$$H = H_0 + U_i, (i = \mathrm{I}, \mathrm{II}, \mathrm{III}). \tag{1}$$

H_0 is the Hamiltonian of the nonreciprocal non-Hermitian SSH chain. U_i denotes the Hamiltonian of imaginary potentials. Regarding H_0, it takes the form

$$H_0 = \sum_n [t_l c^\dagger_{A,n} c_{B,n} + t_r c^\dagger_{B,n} c_{A,n} + t_2 (c^\dagger_{A,n+1} c_{B,n} + c^\dagger_{B,n} c_{A,n+1})]. \tag{2}$$

$c^\dagger_{\alpha,n}(c_{\alpha,n})$ is the creation (annihilation) operator of the particle at site α $(\alpha = A, B)$ of the nth cell. $t_{l(r)} = t_1 \pm \gamma$ are the amplitudes of intracell hoppings. Note that γ is exactly the intracell nonreciprocal coupling strength. Due to the presence of γ, the nonreciprocal non-Hermitian SSH chain is achieved. In addition, t_2 is the amplitude of intercell hopping.

Based on the above Hamiltonian, we would like to introduce $\mathcal{PT}$-symmetric onsite imaginary potentials to observe the property variations of the nonreciprocal non-Hermitian SSH chain, since such potentials enable one to introduce new physics pictures to the topological systems. In this paper, we would like to consider three types of imaginary potential settings, i.e.,

$$\begin{aligned} U_{\mathrm{I}}(\epsilon) &= i\epsilon \left(\sum_n c^\dagger_{A,n} c_{A,n} - c^\dagger_{B,n} c_{B,n} \right), \\ U_{\mathrm{II}}(\epsilon) &= i\epsilon (c^\dagger_{A,1} c_{A,1} - c^\dagger_{B,N} c_{B,N}), \\ U_{\mathrm{III}}(\epsilon) &= i\epsilon \left[\sum_{n=1}^{N/2} (c^\dagger_{A,n} c_{A,n} + c^\dagger_{B,n} c_{B,n}) - \sum_{n=N/2+1}^{N} (c^\dagger_{A,n} c_{A,n} + c^\dagger_{B,n} c_{B,n}) \right]. \end{aligned} \tag{3}$$

It is clearly shown that U_{I} describes the case where imaginary potentials are added on sites A and B in each cell in a periodic way. ϵ corresponds to the magnitude of the imaginary potentials. According to the previous works, positive and negative signs represent the energy gain and loss, respectively, which has already been realized in experiment [22]. For U_{II}, it denotes the case of two imaginary potentials added on the ending sites of the SSH chain. Next, U_{III} shows the alternate case in which the imaginary potentials are added by dividing the SSH chain into two domains. To be concrete, energy gain is assumed to occur in the left-half domain, whereas energy loss occurs in the right-half domain.

When observing the three types of cases, one can find that all of them have the η-pseudo-Hermitian symmetry [51,52], i.e., $\eta H \eta^{-1} = H^\dagger$ with $\eta = I_{\mathrm{off-diag}\,N}$. Therefore, we can claim that such cases have non-Bloch $\mathcal{PT}$ (n$\mathcal{PT}$) symmetry, due to the coexistence of nonreciprocal couplings and $\mathcal{PT}$-symmetric imaginary potentials. Surely, such a kind of symmetry also leads to the appearance of real eigenvalues [52]. Meanwhile, it can be seen that the above Hamiltonians have particle-hole symmetry with $\mathcal{C}H^*\mathcal{C}^{-1} = -H$ $(\mathcal{C} = I_{N/2} \otimes \sigma_z)$, time-reversal symmetry with $\mathcal{T}H^T\mathcal{T}^{-1} = H$ $[\mathcal{T} = \text{off-diag}(1, 1, \ldots, 1) \otimes \text{off-diag}(1, 1, \ldots, 1)\mathcal{K}]$, and chiral symmetry with $\Gamma H^\dagger \Gamma^{-1} = -H$ $(\Gamma = I_{\mathrm{off-diag}\,N/2} \otimes i\sigma_y)$. According to the work [53], we can ascertain the non-Hermitian topological classes of all the three cases. Namely, they belong to the BDI†-class topology.

III. THEORETICAL DERIVATION

According to the Hamiltonian in the above section, we continue to evaluate the skin effect and edge states of our SSH chain. Through this derivation, we aim to give the conditions for the direction, skin degree, and location of the NHSE of the bulk states as well as the localization of the edge states, by presenting the ratio of the relevant parameters. We would like to emphasize that the appearance of skin effect and localized edge states can be described by solving the Schrödinger equation. The details are presented as follows.

To begin with, we assume a left local state to be defined as $\psi_L = \Sigma_i^N L_i |i\rangle$ with a right local state written as $\psi_R = \Sigma_i^N R_i |i\rangle$ (note that in our system, odd i is for site A with even i for site B). Taking the case of ψ_L as an example, we write out the relevant Schrödinger equation $H\psi_L = E\psi_L$. And then, the eigenvalue equations of the left local states under the open boundary condition can be given as

$$X_{L,1} L_1 + t_l L_2 = E L_1, \tag{4}$$

$$t_r L_n + t_2 L_{n+2} + X_{L,n+1} L_{n+1} = E L_{n+1}, n \in [1, N), \tag{5}$$

$$t_2 L_{n-2} + t_l L_n + X_{L,n-1} L_{n-1} = E L_{n-1}, n \in (1, N], \tag{6}$$

$$t_r L_{N-1} + X_{L,N} L_N = E L_N. \tag{7}$$

Equations (4) and (7) are related to the left and right boundary conditions, whereas Eqs. (5) and (6) are for bulk states, with Eq. (5) for odd n and Eq. (6) for even n, respectively. In addition, $X_{L/R,n} = X_{L/R,n}(\epsilon)$ represent the generalized onsite energies of the SSH chain. For instance, in case I of our system, one can understand $X_{L/R,1}(\epsilon) = \pm i\epsilon$. By the

same token, the eigenvalue equations of the right local states can be obtained by changing L_i to R_i. When observing Eqs. (4)–(7), we can find that regardless of the three types of $\mathcal{PT}$-symmetric imaginary potentials, the eigenvalues of the Schrödinger equations are allowed to obey two relationships, i.e., $E = X_{L,1;(R,N)}(\epsilon)$ or $E \neq X_{L,1;(R,N)}(\epsilon)$, respectively (for convenience, the subindex of X will be ignored hereafter).

On the one hand, as the localized edge states arise, their eigenenergies have an opportunity to satisfy the result of $E = X$. Instead, the eigenenergies describe the characteristics of the bulk states. In view of this phenomenon, we can discuss the properties of L_i to present the leading properties of the localized edge states and the bulk-state skin effect. First, when $E = X(\epsilon)$, we can immediately derive $L_n = -t_2/t_r L_{n+2}$, $L_2 = 0$. Furthermore, if the localized edge state exists in this system, the distribution of it must have a threshold value at site m (such as higher-localized edge states $m \in [2, 5]$ and Z) which satisfies $L_{m+1} = 0$, when the maximum site for localized edge state appears on the left. In fact, the absolute value of L_m is basically of the order 10^{-2}, the smallest among L_i. So we can derive

$$|L_1|^2 \propto \left|\frac{t_2}{t_r}\right|^{m-1} |L_m|^2, \tag{8}$$

$$L_n = 0, (n \text{ is even}). \tag{9}$$

This result means that if the eigenvalue of localized edge state satisfies $E = X(\epsilon)$, $|\psi_L|^2$ will have oscillatory value along with the increase of sites to the left direction, accompanied by the occurrence of the state localization on the left if $|t_2| > |t_r|$.

Regarding the localized edge state on the right, we can perform the same analysis about ψ_R. In the presence of the right localized states, the distribution of the local states also has a threshold value at site m' which satisfies $R_{m'-1} = 0$. Just like the left localization case, $R_{m'}$'s absolute value also is around 10^{-2} and is the smallest among R_i. According to this relationship, we can obtain the following result:

$$R_n = 0, (n \text{ is odd}), \tag{10}$$

$$|R_N|^2 \propto \left|\frac{t_2}{t_l}\right|^{N-m'} |R_{m'}|^2. \tag{11}$$

It is obvious that this system has an opportunity to display the right-side localized edge states when $|t_2| > |t_l|$. Up to now, we can find that the localized edge states on the left or right must not be consistent with each other due to $|t_l| \neq |t_r|$. In other words, the difference between t_l and t_r determines the localized edge states in this system. It is easy to understand that if $|t_r| < |t_l|$ ($|t_r| > |t_l|$), for the same $|t_2|$, Eqs. (8) and (11) is more dominant. Obviously, the system intends to display the left (right) localized edge state, in the case of $|t_2| > |t_r|$ ($|t_2| > |t_l|$). Moreover, the left (right) localized edge state can be ascertained under the condition of $|t_l| > |t_2| > |t_r|$ ($|t_r| > |t_2| > |t_l|$). However, if $|t_2| \geqslant |t_l| > |t_r|$ or $|t_2| \geqslant |t_r| > |t_l|$, the competition between Eqs. (8) and (11) will become uncertain, so localized edge states have the possibility to exhibit the double-direction localization, with the critical condition $|t_2| \approx |t_l|$ ($|t_2| \approx |t_r|$) where the localization phenomenon could be destroyed.

On the other hand, when $E \neq X(\epsilon)$, the localization behaviors of the eigenstates can be viewed as the skin effect of the bulk states and some edge states. In such a case, the above derivation can be performed in an alternate way. Taking the left-side skin effect as an example, considering there is $L_{m+1} = 0$, we can write out the result that $L_{m-1} = \frac{(E-X)}{t_r} L_m$. Substituting this result in Eqs. (4)–(7), one can find that $L_{m-2} = \frac{(E-X)^2 - t_l t_r}{t_2 t_r} L_m$. Next, the general form of L_{m-q} can be expressed, i.e.,

$$L_{m-q} = \frac{\sum_j P_j(t_2, t_l, t_r)(E-X)^j}{t_2^{[q/2]} t_r^{[(q+1)/2]}} L_m. \tag{12}$$

$\sum_j P_j(t, t_l, t_r)(E-X)^j$ is the polynomial of $(E-X)$ and P_j is a function about t_l, t_r, and t_2. The maximum value of index j is equal to q, but $j = 1, 3, 5, \ldots, q$ when q is odd and $j = 0, 2, 4, \ldots, q$ when q is even. Meanwhile, the polynomial $\sum_j P_j(t, t_l, t_r)(E-X)^j$ is different for j odd or even. For odd j,

$$\begin{aligned}
&\sum_j P_j(t, t_l, t_r)(E-X)^j \\
&\quad = (E-X)^q - \left[\frac{(q-1)}{2} t_l t_r + \frac{(q-1)}{2} t^2\right](E-X)^{q-2} \\
&\qquad + \ldots + P_j(E-X)^j + \ldots + P_1(E-X),
\end{aligned}$$

in which $P_1 = -[t^{q-1} + t^{q-3} t_l t_r + \ldots + t^{q-s} t_l^{(l-1)/2} t_r^{(l-1)/2} + \ldots + t_l^{(q-1)/2} t_r^{(q-1)/2}]$.

For even j, we can obtain

$$\begin{aligned}
&\sum_j P_j(t, t_l, t_r)(E-X)^j \\
&\quad = (E-X)^q - \left[\frac{q}{2} t_l t_r + \frac{(q-2)}{2} t^2)\right](E-X)^{q-2} \\
&\qquad + \ldots + P_j(E-X)^j + \ldots + P_1,
\end{aligned}$$

with $P_1 = -t_l^{q/2} t_r^{q/2}$. Note that if $|E-X|$ is small, we can drop all the terms that include $(E-X)$. In such a case, Eq. (12) changes to be

$$L_{m-q} \approx \frac{t_l^{q/2}}{t_2^{q/2}} L_m. \tag{13}$$

For the right-side skin effect, in the same way, we derive

$$R_{m+q} = \frac{\sum_j P'_j(t_2, t_l, t_r)(E-X)^j}{t_2^{[q/2]} t_l^{[(q+1)/2]}} R_m. \tag{14}$$

If $|E-X|$ is small enough, there will be

$$R_{m+q} \approx \frac{t_r^{q/2}}{t_2^{q/2}} R_m. \tag{15}$$

In Eqs. (12)–(15), it can be readily found that the large value of $|E-X|$ is certain to induce the occurrence of the skin effect. If $|E-X|$ is small, the skin effect will be relatively weak. Similar to the case of $E = X$ which displays the localized edge states, the difference between t_l and t_r determines the skin effect to occur on the left or right in this SSH chain. For the case of large $|E-X|$, if $|t_l| > |t_r|$

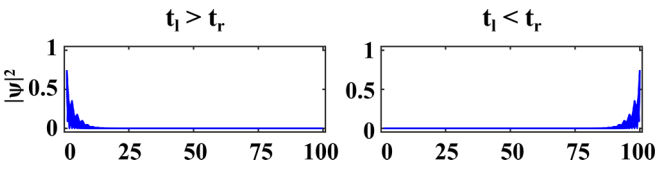

FIG. 2. The direction of the skin effect in the nonreciprocal SSH chain is highly related to the ratio of t_l and t_r. Relevant parameters are taken as $\epsilon = 0, t_2 = 1.0$. (a) $t_l = 1.5$ and $t_r = 0.5$ for $t_l > t_r$. (b) $t_l = 0.5$ and $t_r = 1.5$ for $t_l < t_r$.

($|t_l| < |t_r|$), Eqs. (12) and (14) is more competitive for the same E, so the system intends to display the left (right) skin effect. To check this conclusion, we present the numerical results in Fig. 2. One can readily find the skin effect determined by the ratio of t_l and t_r. However, for some special states, $|E - X|$ may become very small. In such a case, according to Eqs. (13) and (15), we can know that if $|t_l| > |t_2| > |t_r|$ ($|t_r| > |t_2| > |t_l|$), such states must be manifested as the left (right) skin characteristics. Surely, for the edge states when $E \neq X(\epsilon)$, if $|t_2| \approx |t_r|$ ($|t_2| \approx |t_l|$), the localization could be suppressed seriously, similar to the result of $E = X$.

The above analysis helps us to understand the localized edge states and the bulk-state skin effect under the conditions of $E = X$ and $E \neq X$, respectively. In practice, for the cases of $U_{\rm II}$ or $U_{\rm III}$, additional boundaries or domain walls are formed in the SSH chain, and then the energies of some states are allowed to satisfy $E = X_a$ and $E \neq X_b$ simultaneously (X_a and X_b are the onsite energies beside the boundary or domain wall). In that case, taking the left skin effect as an example, we consider the threshold site to be $m = n' + q$ and $E \neq X_b$ exists before site n'. From Eqs. (4)–(7) we have

$$\begin{aligned}
&\cdots \\
t_2 L_{n'-2} + t_l L_{n'} &= (E - X_b) L_{n'-1}, \\
t_r L_{n'-1} + t_2 L_{n'+1} &= (E - X_b) L_{n'}, \\
t_2 L_{n'} + t_l L_{n'+2} &= 0, \\
t_r L_{n'+1} + t_2 L_{n'+3} &= 0, \\
&\cdots \\
t_r L_{n'+q-2} + t_2 L_{n'+q} &= 0.
\end{aligned}$$

This exactly means that $L_{n'} = (t_r L_{n'-1} + t_2 L_{n'+1})/(E - X_b)$ and $L_{n'-1} = (t_2 L_{n'-2} + t_l L_{n'})/(E - X_b)$. In the presence of large $|E - X_b|$, e.g., $|E - X_b| \gg t_2$, $L_{n'}$ has an opportunity to decay rapidly following the decay of $L_{n'+1}$ and $L_{n'-1}$. At the same time, $L_{n'-1}$ decays following $L_{n'}$ and $L_{n'-2}$ in such a case. Thus, the magnitude of $L_{n'+1}$ must be much larger than $L_{n'-1}$, and $L_{n'-1}$ can be ignored. This allows us to consider L_i in front of $L_{n'-1}$ to be equal to zero. Then, the relationship between $L_{n'+1}$, $L_{n'+3}$, $L_{n'}$, and $L_{n'+1}$ will be simplified as

$$\left|\frac{L_{n'+1}}{L_{n'+q}}\right|^2 = \left(\frac{t_2}{t_r}\right)^{q-1}, \tag{16}$$

$$\frac{L_{n'}}{L_{n'+1}} = \frac{t_2}{E - X_b}. \tag{17}$$

Obviously, the magnitude of L_i will be decreased rapidly at site n'. Therefore, the wave function cannot pass through site n' and there must be a local location on $L_{n'+1}$ which can be called a local point (LP) mainly working for the edge states. Here, we set LP > 0 (LP < 0) which originates from positive (negative) imaginary potentials. For the special case that the system has a large q, i.e., a domain wall which is known as the boundary, the LP changes to be the boundary point (BP). In this sense, the system edges can also be recognized as BPs. Different from the LPs, BPs mainly affect the bulk states. Thus we just talk about the BP in the case of the domain wall.

Following the above discussion, we next would like to clarify the critical locations of the localized states. For the Hamiltonian H with eigenvalues E_i, we rewrite the corresponding secular equation, i.e.,

$$\begin{aligned}
&\det|EI - H| \\
&\quad = [E_1 - (X_1 - \delta_1)] \ldots [E_i - (X_i - \delta_i)] \\
&\qquad \times \ldots [E_{N-1} - (X_{N-1} - \delta_{N-1})][E_N - (X_N - \delta_N)] \\
&\quad = \prod_i [E_i - (X_i - \delta_i)] = 0.
\end{aligned} \tag{18}$$

Here I is the identity matrix and $\delta_i \in C$. δ_i is an adjustable parameter to fit E_i and X_i is the potential energy of site i, with their relationship of $|{\rm Im}(\delta_i)| \leqslant |{\rm Im}(X_{\rm max})| = \epsilon$. It can be understood that for edge modes, ${\rm Re}(X_i) = {\rm Re}(\delta_i)$, so $|X_i| \geqslant |\delta_i|$, indicating that ${\rm sgn}(X_i - \delta_i) = {\rm sgn}(X_i)$. Furthermore, the states which have the result of $\delta = 0$ are certain to be localized edge states. Thus from Eq. (18), we can find that the localized edge states must be located at the site where $X_i = E_i$, and the edge states at the domain wall must be located at the site where ${\rm sgn}(X_i) = {\rm sgn}(E_i)$, i.e., ${\rm sgn}(E_i) = {\rm sgn(LP)}$ or ${\rm sgn(BP)}$ combining with the foregoing. In view of this fact, we can consider that the locations of localized edge states can be modulated by setting the proper X_i, e.g., the imaginary potentials. This also means that the positions of the localized edge states are not necessarily identical with the skin effect, in the presence of proper imaginary potentials.

Now, we can make a brief conclusion from the above discussions as follows.

A. $\mathbb{C}_1$

For $t_l > t_r$ ($t_l < t_r$), the system display the left (right) skin effect. In the case of $E = X$, Eqs. (8) and (11) are only for localized edge states, whereas if $E \neq X$, Eqs. (12) and (14) will be used to describe the skin effect of bulk states, with Eqs. (13) and (15) related to the case of small $|E - X|$.

B. $\mathbb{C}_2$

The effects of the two mechanisms, i.e., the nonreciprocal coupling as well as imaginary potentials, on the edge and bulk states of the system are shown in Table I. The label "$|t_l| > t_2 > |t_r|$, NHSE $\Rightarrow$ left (right)" means if the system has $|t_l| > t_2 > |t_r|$ then the skin effect of bulk states will arise at the left (right) boundary, i.e., the direction of the NHSE is on the left (right) side, and other labels represent similar meanings. The label "Direction of NHSE" means that the local direction of the edge state is the local direction of NHSE, i.e., the stronger effect of the nonreciprocal coupling on the local direction of the edge state. The label "Direction of ${\rm sgn}(E) = {\rm sgn(LP)}$" means that the edge states whose

TABLE I. The specific results for judging the localization directions of the edge and bulk states under the action of nonreciprocal coupling and imaginary potentials. Our conditions are divided into the Hopping conditions and the potential conditions. Combining these two conditions, we can prejudge the local direction of edge states. The global LP is the system with the imaginary potentials in all sublattices, such as the case of U_{I}. The regional LP is the system with the imaginary potentials in some part of sublattices, such as the cases of U_{II} and U_{III}.

Potential conditions \ Hopping conditions			$\lvert t_l\rvert>\lvert t_2\rvert>\lvert t_r\rvert$, *NHSE⇒Left*	$\lvert t_l\rvert>\lvert t_r\rvert>\lvert t_2\rvert$, *NHSE⇒Left*	$\lvert t_2\rvert>\lvert t_l\rvert>\lvert t_r\rvert$, *NHSE⇒Left*
			$\lvert t_r\rvert>\lvert t_2\rvert>\lvert t_l\rvert$, *NHSE⇒Right*	$\lvert t_r\rvert>\lvert t_l\rvert>\lvert t_2\rvert$, *NHSE⇒Right*	$\lvert t_2\rvert>\lvert t_r\rvert>\lvert t_l\rvert$, *NHSE⇒Right*
Global *LP*	$E=X$		*Direction of NHSE*	*Direction of* sgn(E) = sgn(LP)	
	$E\neq X$		*Direction of NHSE*		
Regional *LP*	$E=X$		*Direction of NHSE*	*Direction of* sgn(E) = sgn(LP)	
	$E\neq X$	Small $\lvert E-X\rvert$	*Direction of* sgn(E) = sgn(LP)		
		Large $\lvert E-X\rvert$	*Direction of NHSE*	*Direction of* sgn(E) = sgn(LP)	

eigenenergies are positive (negative) will be localized at the position of positive (negative) LP. The modulation mechanism of imaginary potentials, i.e., the locations of the LPs, have stronger effects on the local directions of the edge states.

C. $\mathbb{C}_3$

For the edge states, whether $E = X$ or $E \neq X$, when the system satisfies $|t_r| \approx |t_2|$ or $|t_l| \approx |t_2|$, the localization of edge states will be destroyed.

IV. NUMERICAL RESULTS AND DISCUSSIONS

Based on the theoretical framework in the above two sections, we proceed to carry out numerical calculations to present the skin effects and localized edge states in the three cases of the nonreciprocal non-Hermitian SSH chain in the presence of $\mathcal{PT}$-symmetric imaginary potentials.

A. Case I

1. Energy-band structure

We first concentrate on case I where the Hamiltonian is written as $H = H_0 + U_{\mathrm{I}}$. The spectra of the energy-band structures are shown in Figs. 3(a)–3(c) with the variable t_1 for $\epsilon = 0$, 0.15, and 0.85, respectively. Figure 3(a) is the original band structure of the nonreciprocal SSH chain [42]. In Fig. 3(b) we find that in the case of $\epsilon = 0.15$, the zero-energy modes in the topologically nontrivial region begin to display the imaginary energies $\pm i\epsilon$. Meanwhile, the band crossing points are magnified and changed to be two "conglutination" regions, which can be considered as the so-called zero-gap phase. The result means that the n$\mathcal{PT}$ symmetry of this region has been broken by the imaginary potentials. Next in Fig. 3(c), it is shown that with the gradual increase of imaginary potential strength, the two-side zero-gap phase regions are magnified obviously. Especially in the case of $\epsilon = 0.85$, the original topologically trivial regions are eliminated. And also, a new zero-gap phase region arises in the vicinity of $t_1 = 0$. Here we call it the central zero-gap phase.

In order to further present the key role of $\mathcal{PT}$-symmetric imaginary potentials in case I, we take $t_1 = 0.2$ and plot the real and imaginary parts of energy as functions of imaginary potential strength ϵ. It can be clearly found in Fig. 3(d) that with the increase of ϵ, the magnitude of the real part of energy tends to be decreased, accompanied by the increase of the spectral widths. Accordingly, in the case of $\epsilon = 0.77$, the two branches of the real energy merge into one, and the band gap disappears. On the other hand, the increase of ϵ enlarges the range of the imaginary part of the energy of the bulk states. As a result, in the critical case of $\epsilon = 0.77$, the imaginary part of energy is divided into two branches. We can thus consider this point to be the exceptional point of the phase transition of bulk states. Regarding the purely imaginary states, the imaginary part of energy appears when ϵ is not equal to zero. This indicates that the system is located in the regime of n$\mathcal{PT}$-symmetry breaking.

2. Topological condition and phase diagram

In Fig. 4, we figure out the phase diagram of the topological phase transition in case I, caused by the increase of ϵ. Before the numerical calculation, we would like to present our analytical discussion. To perform calculation, we consider the Hamiltonian under the periodic boundary condition and express it in the GBZ [52], i.e.,

$$H_\beta = \begin{bmatrix} i\epsilon & t_1+\gamma+t_2\beta^{-1} \\ t_1-\gamma+t_2\beta & -i\epsilon \end{bmatrix}. \tag{19}$$

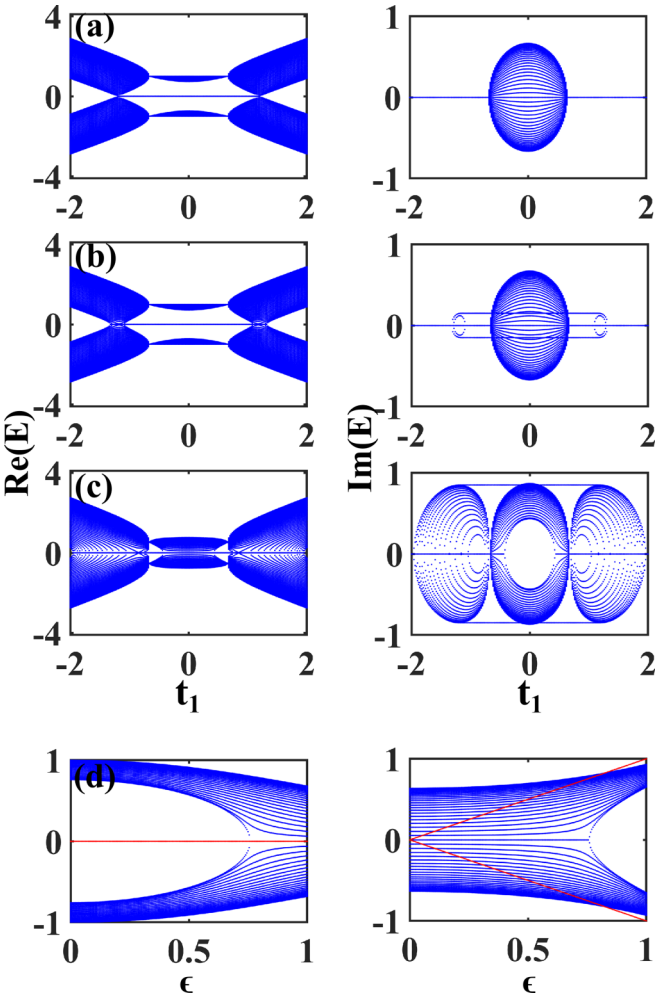

FIG. 3. (a)–(c) Spectra of the real and imaginary parts of the energy-band structures. Parameters are taken as $t_2 = 1.0$, $\gamma = 2/3$, and (a) $\epsilon = 0$, (b) $\epsilon = 0.15$, and (c) $\epsilon = 0.85$. (d) Real and imaginary parts of energy as functions of ϵ. Relevant parameters are set to be $t_1 = 0.2$, $t_2 = 1.0$, and $\gamma = 2/3$.

In this equation, $\beta = re^{ik}$ and $r = \sqrt{|t_1 - \gamma|/|t_1 + \gamma|}$. It is not difficult to find that the formulation of the characteristic equation of H_β obeys the form of $f(\beta) = \Sigma_n t_n \beta^n$. Then considering $f(\beta) = 0$, we can obtain the result that

$$\beta_{1,2} = \frac{T \pm \sqrt{4t_2^2(\gamma^2 - t_1^2) + T^2}}{2t_2(t_1 + \gamma)}, \tag{20}$$

where $T = \epsilon^2 - t_1^2 - t_2^2 + \gamma^2$. According to the previous works [52,53], when $|\beta_j| = |\beta_{j+1}|$, we can get the phase transition conditions, i.e.,

$$t_1 = \pm\sqrt{(t_2 \pm \epsilon)^2 + \gamma^2} \quad |t_1| > |\gamma|, \tag{21}$$

$$\epsilon = \sqrt{t_1^2 + t_2^2 - \gamma^2} \quad |t_1| < |\gamma|. \tag{22}$$

In Figs. 4(a) and 4(b), we plot the curves of $|\beta|$ as a function of t_1 in the case of $\epsilon = 0.15$ and 0.85, respectively. It can be readily observed that there are two regions manifested as $|\beta_1| = |\beta_2|$ for $\epsilon = 0.15$, whereas for $\epsilon = 0.85$ an additional point of $|\beta_1| = |\beta_2|$ appears at $t_1 \approx \pm 0.4$ except the two

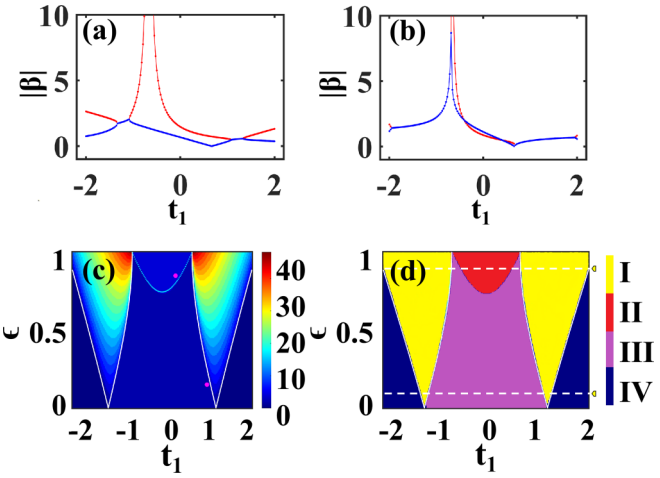

FIG. 4. (a), (b) The curves of β_j as a function of t_1 in the cases of $\epsilon = 0.15$ and 0.85, respectively. (c) The distribution of edge state number with the change of ϵ and t_1. Two pink dots are ($t_1 = 0.5$, $\epsilon = 0.9$) and ($t_1 = 1.0$, $\epsilon = 0.15$). (d) Phase diagram according to panel (c) with the change of ϵ and t_1.

similar regions. We find that Eqs. (21) and (22) can consist with the phase transition condition of the two-side zero-gap phase and the central zero-gap phase, respectively, which correspond to the results in Figs. 3(b) and 3(c).

With the help of the above derivation, in Fig. 4(c) we present the distribution of edge-state number in different phase regions. Equations (21) and (22) describe the white and cyan lines. We can find that the numbers of two types of zero-gap phases are different from each other, corresponding to different physical properties. According to Fig. 4(c), the system has four phase regions, i.e., the two-side zero-gap phase (yellow I), the central zero-gap phase (red II), and the topologically nontrivial (pink III) and trivial (blue IV) phases, as shown in Fig. 4(d).

3. Skin effect and topological edge states

Next, to illustrate the NHSE and the topological edge states in case I, we pay attention to the density-of-state (DOS) distribution of the bulk states and the edge states. The relevant parameters correspond to the two pink dots in Fig. 4(c).

In Fig. 5(a), we present the DOS distribution of the bulk states and topological edge states in the central zero-gap phase. For the bulk states, the system exhibits the NHSE in the left direction because of $\mathbb{C}_1$. For the edge states, they display a different localization effect. To be specific, the edge states are localized on the left side when $E = \pm 0.9000i = X$ and the localization in the case of $E = -0.9000i$ is worse than that of $E = 0.9000i$ in Figs. 5(a)(i) and 5(a)(ii). When $E = \pm 0.1133i \neq X$, the edge states are also localized on the left side, just the same as the direction of NHSE. In the topologically nontrivial region [see Fig. 5(b)], the topological edge states and skin effect of the bulk states are relatively well defined and have the same localized direction.

Based on the above phenomena of localization, we can explain the conclusions in Sec. III. Whether $t_1 = 0.5$, $\epsilon = 0.90$ ($|t_l| = 1.166$ and $|t_r| = 0.166$) or $t_1 = 1.0$, $\epsilon = 0.15$ ($|t_l| = 1.666$ and $|t_r| = 0.344$), the hopping terms satisfy the

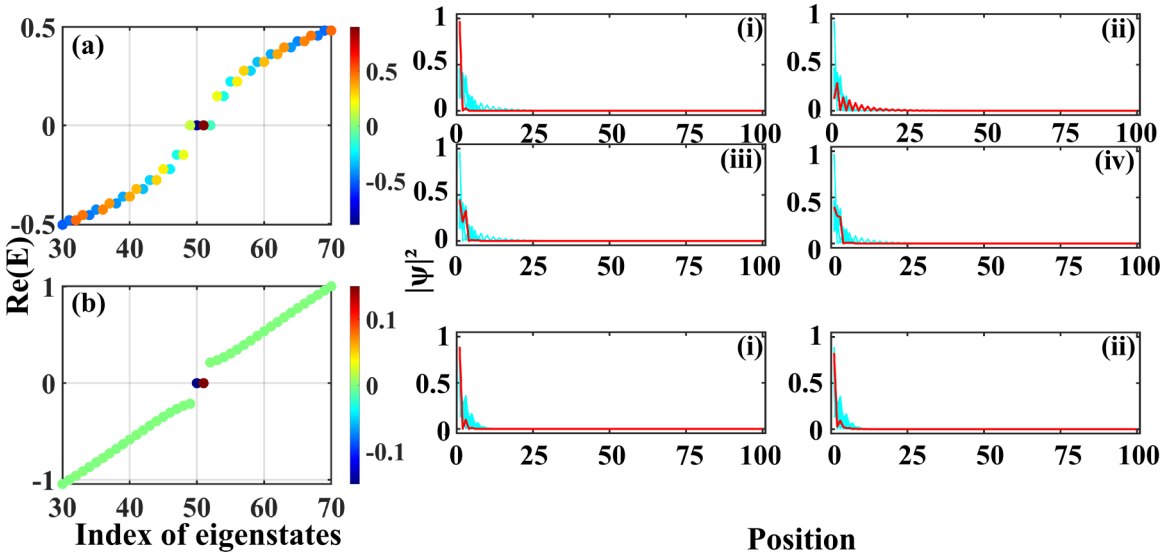

FIG. 5. The index of eigenstates and density-of-state distribution of the bulk states and topological edge states (a) in the central zero-gap phase ($t_1 = 0.5$, $\epsilon = 0.90$) and (b) in the topological phase ($t_1 = 1.0$, $\epsilon = 0.15$). In panels (a) and (b), the colorscale corresponds to the value of the imaginary part of energy. Eigenenergies of edge states for panel (a) are taken as (i) $E = 0.9000i$, (ii) $E = -0.9000i$, (iii) $E = 0.1133i$, and (iv) $E = -0.1133i$; for panel (b) they are taken as (i) $E = 0.1500i$ and (ii) $E = -0.1500i$. The red lines describe the density-of-state distribution of the edge states, and cyan lines denote the skin effect of the bulk states.

relationship $t_l > t_2 > t_r$. Taking the result in Fig. 6(a)(i) as an example, the energy of the edge state belongs to the type of $E = X$. Supposing $m = 5$ and putting such a condition into Eq. (8), one has $|L_1|^2 = |\frac{t_2}{t_r}|^4 |L_5|^2$. With the help of $|L_1|^2 + |L_3|^2 + L_5^2 = 1$, we can obtain the result of $L_1 \approx 0.868$, $L_3 \approx 0.116$, and $L_5 \approx 0.016$. These results are the same as the values in Fig. 6(a)(i). Therefore, one can find that our conclusions in Sec. III are correct. For the case in Fig. 6(a)(ii), although the eigenenergy of the edge state is a negative imaginary number, at this point the localization of the edge state is modulated by the NHSE, therefore it is still manifested as the left-side localization. Also, with the condition $|t_2| \approx |t_r|$, the effect of localization is not well defined, which has already been discussed regarding $\mathbb{C}_3$. From the above results, we can prove that our conclusions in Sec. III are reasonable.

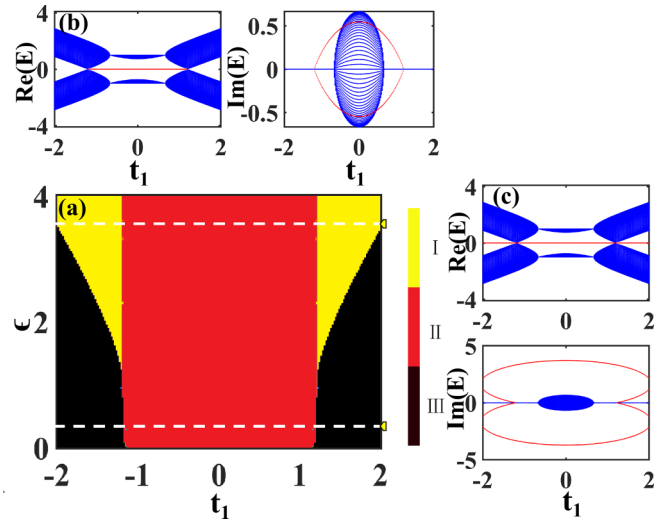

FIG. 6. (a) Phase diagram with the change of ϵ and t_1. The spectra of energy bands are (b) $\epsilon = 0.4$ and (c) $\epsilon = 3.6$.

B. Case II

In this subsection, we turn to the investigation of case II with its Hamiltonian written as $H = H_0 + U_{\mathrm{II}}$. In such a case, the imaginary potentials are applied to the end sites of the SSH chain. The phase diagram and the band structures for some typical cases are shown in Fig. 6.

1. Phase diagram and energy band

Figure 6 displays the phase diagram and specific energy bands. From the phase diagram, we see that with the increase of ϵ, the original topologically nontrivial region (region II) is not changed and the topologically trivial region (region III) is narrowed obviously. Between the topologically nontrivial and trivial regions, a new type of phase region comes into being, in the case of rising ϵ. Such a phase region is widened apparently in this process.

To further clarify the band structure of case II of the SSH chain, we take two cases to present the real and imaginary parts of energy, as shown in Figs. 6(b) and 6(c). For the case of small ϵ, e.g., $\epsilon = 0.4$ [see Fig. 6(b)], in the range of $t_1 \in [-1.21, 1.21]$, the edge states have imaginary energy $\mathrm{Im}(E) \neq 0$. Since the topological states are located at the ends of the SSH chain, the application of imaginary potentials is certain to modify the energies of the edge states. In the region of $1.21 < |t_1| < 2.0$, all the eigenenergies are real. Thus, the states are protected by the n$\mathcal{PT}$ symmetry. With the increase of ϵ, the edge states are not ended at the band-crossing points, but penetrate into the topologically trivial region. In the extreme case where $\epsilon = 3.6$, in Fig. 6(c) we see that the edge states penetrate into the topologically trivial region, and the imaginary part of energy obtains the larger magnitude. One

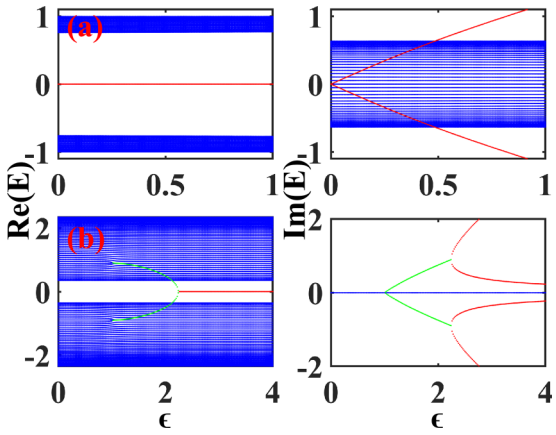

FIG. 7. Real and imaginary parts of energy with (a) $t_1 = 0.2$ and (b) $t_1 = 1.5$. We can clearly find that two bulk states become edge states induced by imaginary potential.

can also find that edge states have two pairs of the imaginary part of energy. This means that the two types of edge states possess different properties. In Fig. 7, we present the variation of the real and imaginary parts of energy with the increase of the imaginary potential strength, for further describing the role of the imaginary potentials in modulating the respective states. As shown in Figs. 7(a) and 7(b) where $t_1 = 0.2$ and 1.5, we can clearly observe that the two types of phase regions have different properties. To be specific, in the case of $t_1 = 0.2$ [see Fig. 7(a)], the edge states obtain the imaginary part of energy when $\epsilon > 0$, which is proportional to the value of ϵ in a linear way. It means that the system is located in the phase of n$\mathcal{PT}$ symmetry breaking. When $t_1 = 1.5$, in Fig. 7(b) it shows that from the imaginary part of energy, the system undergoes two n$\mathcal{PT}$-symmetry phase transitions. The first phase transition is at $\epsilon_{c1} = 1.00$. In the region of $\epsilon \in [0, 1.00]$, all eigenenergies are real and belong to the n$\mathcal{PT}$-symmetry-protected phase. In the region of $\epsilon \in [1.0, 2.24]$, the system has nonzero isolated states in the bulk band and gradually enters into the energy gap [see the green line in Fig. 7(b)]. The second phase transition occurs at $\epsilon_{c2} = 2.24$. The nonzero isolated states become degenerate into purely imaginary edge states. The imaginary part of energy experiences new splitting at ϵ_{c2}.

2. *Skin effect and topological edge states*

Next, we plot the eigenenergy and DOS spectra, by taking the cases of $t_1 = 0.5$ and 1.9 with $\epsilon = 3.6$. According to the energy spectra in Fig. 6(c), whether $t_1 = 0.5$ or 1.9, the edge states do not satisfy $E = X$. Thus, they belong to the case of $E \neq X$. First, when the case of $t_1 = 0.5$, we can derive $t_l = 1.166$ and $|t_r| = 0.166$. For the bulk states, because of $t_l > t_r$, the system has the left skin effect which is consistent with $\mathbb{C}_1$ in Sec. III. For the edge states, we can find that the localization of $E = +(-)3.6495i$ occurs on the left (right) side of the system [see Figs. 8(b)(i) and 8(b)(ii)]. For the new phase, such as $t_1 = 1.9$, $t_l = 2.566$, and $t_r = 1.233$, we see that the edge states of $E = 2.4317i$ and $0.8906i$ are localized at the left boundary of the system, whereas the edge states of $E = -2.4317i$ and $-0.8906i$ are localized at the right boundary of the system. In addition, the bulk states display the left-direction skin effect because of $t_l > t_r$.

Using the same method, the reason for localization phenomena can be explained by the conclusion regarding $\mathbb{C}_2$. In the presence of U_{II}, $+i\epsilon$ is set on the left side and $-i\epsilon$ is set on the right side, thus the direction of LP > 0 (LP < 0) occurs on the left (right) side. For the case of $t_1 = 0.5$, the hopping terms satisfy $t_l > t_2 > |t_r|$ and the $|E - X|$ value of edge states is large. According to Table I, the localization of edge states is adjusted by the direction of the LP at this point. Therefore, the positive-imaginary energy edge state is localized in the direction of LP > 0, i.e., on the left side.

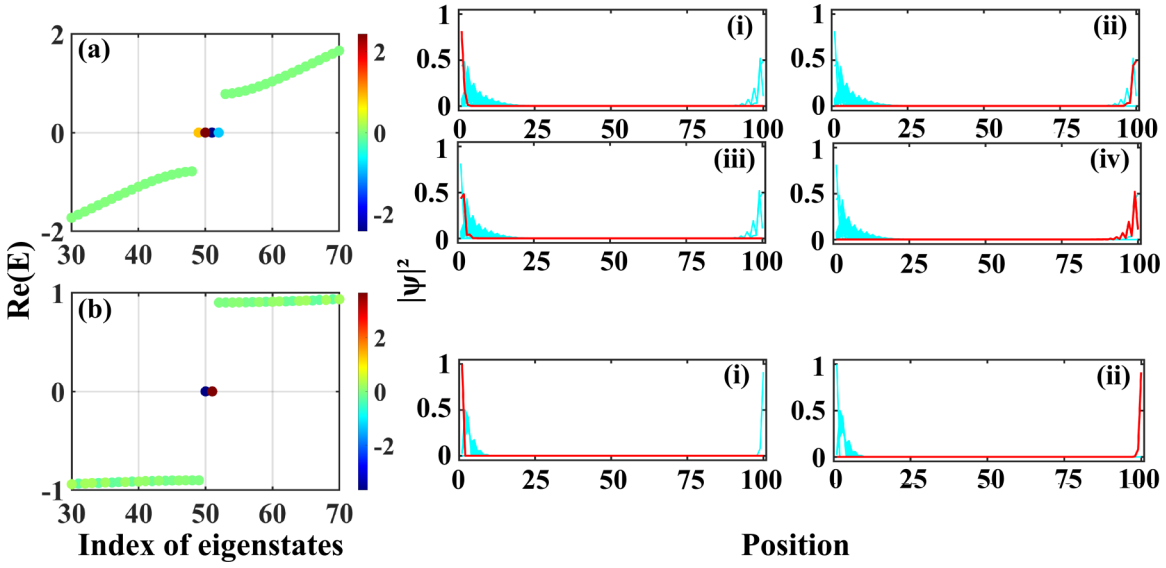

FIG. 8. Index of eigenstates and DOS selected from (a) phase region II ($t_1 = 1.9$, $\epsilon = 3.6$) and (b) phase region I ($t_1 = 0.5$, $\epsilon = 3.6$). The eigenvalues of edge states are [(a)(i)–(a)(iv)] $E = 2.4317i$, $-2.4317i$, $0.8906i$, and $-0.8906i$ and [(b)(i), (b)(ii)] $E = 3.6495i$ and $-3.6495i$. Because there is a negative imaginary potential on the right edge which creates a LP for negative energy, negative-energy edge states localize at the right edge.

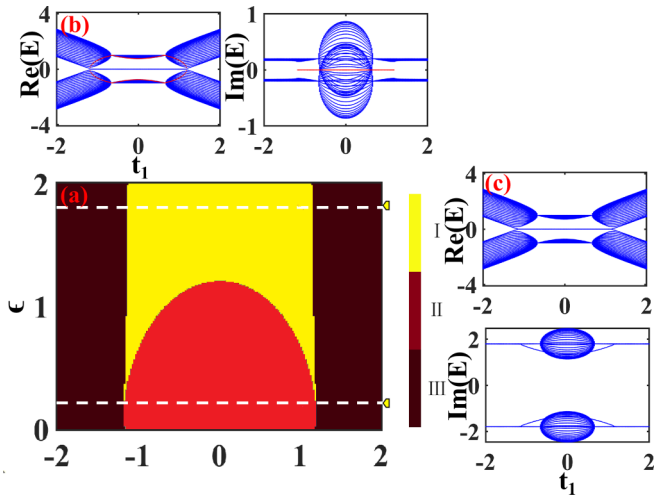

FIG. 9. (a) Phase diagram with the change of ϵ and t_1. Two red dots are ($t_1 = 1.0, \epsilon = 0.2$) and ($t_1 = 1.0, \epsilon = 1.8$). The energy-band spectra are (b) $\epsilon = 0.2$ and (c) $\epsilon = 1.8$.

The same results can be seen in Fig. 8(b)(i). In the same way, for the case of $t_1 = 1.9$, the system satisfies $t_l > t_r > t_2$. From Table I, we know that no matter whether the energy of the edge state belongs to large $|E - X|$ or small $|E - X|$, its local direction is driven by the LP direction. Therefore, the positive-imaginary energy edge state is localized on the left side (direction of LP > 0), and the negative-imaginary energy edge state is localized on the right side (direction of LP < 0). The details can be observed from the results of $E = 2.4317i$ and $-0.8906i$ in Fig. 8.

We can also verify them with the help of numerical results. In case II, we have $X_{i=2\to N-1} = 0$. For the situation of $t_1 = 0.5$, according to $\mathbb{C}_1$, we consider $m = 2$ and put it into Eqs. (4), (5), and (12) and we can obtain the result that $|L_1|^2 = \frac{1}{|t_2/E|^2+1}$ and $E \approx i\epsilon - i(\frac{t_1^2-\gamma^2}{\epsilon})$ for the relatively large ϵ. According to the above formula, it can be found that $L_1 \approx 0.997$, and the edge state is localized on the left side with the energy given as $E \approx 3.65i$.

C. Case III

Following the discussion about cases I and II, we continue to carry out the study on case III with the system's Hamiltonian written as $H = H_0 + U_{\mathrm{III}}$. In such a case, energy gain occurs in the left domain, and energy loss appears in the right domain, thus one domain wall is formed at the middle of the SSH chain.

1. Phase diagram and energy-band structure

In Fig. 9(a), we plot the phase diagram and real and imaginary energy spectra of specific cases. From the phase diagram, the system has three phase regions. With the increase of ϵ, the topologically trivial region (region III) does not undergo any clear change, whereas the topologically nontrivial region (region II) displays phase transition, with the phase boundary close to the relationship of $\epsilon = \sqrt{-t_1^2 + t_2^2 + r^2}$. With the increase of ϵ, the new phase region appears (region I). In Figs. 9(b) and 9(c), we take $\epsilon = 0.2$ and 1.8, respectively, to investigate the spectra of the real and imaginary parts of energy. First, in the case of $\epsilon = 0.2$ in Fig. 9(b), the imaginary potentials induce new pure real energy isolated states to appear in the regions of the bulk states. When imaginary potentials are enhanced, such isolated states tend to be squeezed into the band gap in the topologically nontrivial region. The results in Fig. 9(c) show that in the case of $\epsilon = 1.8$, the degeneracy occurs in the whole topologically nontrivial region. Accordingly, our system obtains another two edge states from the bulk states. Moreover, the imaginary part of energy is not purely real, and the system is always in the broken n$\mathcal{PT}$-symmetry phase.

2. Skin effect and localized edge states

Similarly, we would like to present the localization of the edge states in Fig. 10. In the case of $t_1 = 1.0$, $t_l = 1.666$ and $t_r = 0.334$. The presence of the domain wall causes the system to have a BP at $j = 51$, according to the conclusion of Sec. III. When the effect of ϵ is strong, the BP and LP coincide at the middle of the chain based on Sec. III. Thus, for the bulk states, the left boundary and the site $j = 51$ domain-wall boundary can also have skin effect, according to $\mathbb{C}_1$. For the edge states, two types of phase regions have different results. To be specific, when $\epsilon = 0.2$ in region II [see Fig. 10(b)], the inclusion of weak imaginary potentials leads to the relatively weak BP effect, so the edge states of $E = \pm 0.2000i$ are localized on the left side of the system. In region I, the system has four edge states. At this point the BP effect is strong enough, therefore the edge states of $E = \pm 1.8000i$ and $\pm 1.6720i$ are localized at the left boundary and BP, that is, the direction of skin effect.

In the same way, we can use the conclusion in Sec. III to explain the phenomena. For the case of $t_1 = 1.0$, the hopping term satisfies $t_l > t_2 > |t_r|$. Observing the structure of Hamiltonian H, one can clearly find that the direction of NHSE is on the left side, and another direction of NHSE is in the middle of chain $j = 51$ (BP), based on the conclusion in Sec. III. When the energy of the edge state belongs to $E = X$, according to Table I, the localization direction of the edge state is mainly adjusted by the NHSE, thus the case of $E = \pm 0.2000i$ and $\pm 1.8000i$ can display phenomena like in Fig. 10. When the edge state satisfies $E \neq X$ and large $|E - X|$, such as $E = \pm 1.6720i$, in the region of $t_l > t_2 > t_r$, the direction of the edge state can also be adjusted by the LP (BP).

D. Prediction of edge-state location

Following the above discussion, we can verify that the three conclusions regarding $\mathbb{C}1$–$\mathbb{C}3$ can be used to predict the localization directions of edge states and skin effect of bulk states. In order to validate the precision of our conclusions, we introduce two constructions: $U_1'(\epsilon) = -i\epsilon(\sum_n c_{A,n}^\dagger c_{A,n} - c_{B,n}^\dagger c_{B,n})$ and $U_2'(\epsilon) = i\epsilon(\sum_{n=1}^{N/4} c_n^\dagger c_n - \sum_{n=N/4+1}^{N/2} c_n^\dagger c_n + \sum_{N/2+1}^{3N/4} c_n^\dagger c_n - \sum_{n=3N/4+1}^{N} c_n^\dagger c_n)$.

For U_1', when $t_1 = 0.2$, there will be $t_l = 0.866$ and $|t_r| = 0.466$, so there will be $t_2 > t_l > |t_r|$. For the bulk states, the direction of skin effect will be on the left because of $|t_l| > |t_r|$ according to $\mathbb{C}_1$. Regarding the edge states, the imaginary

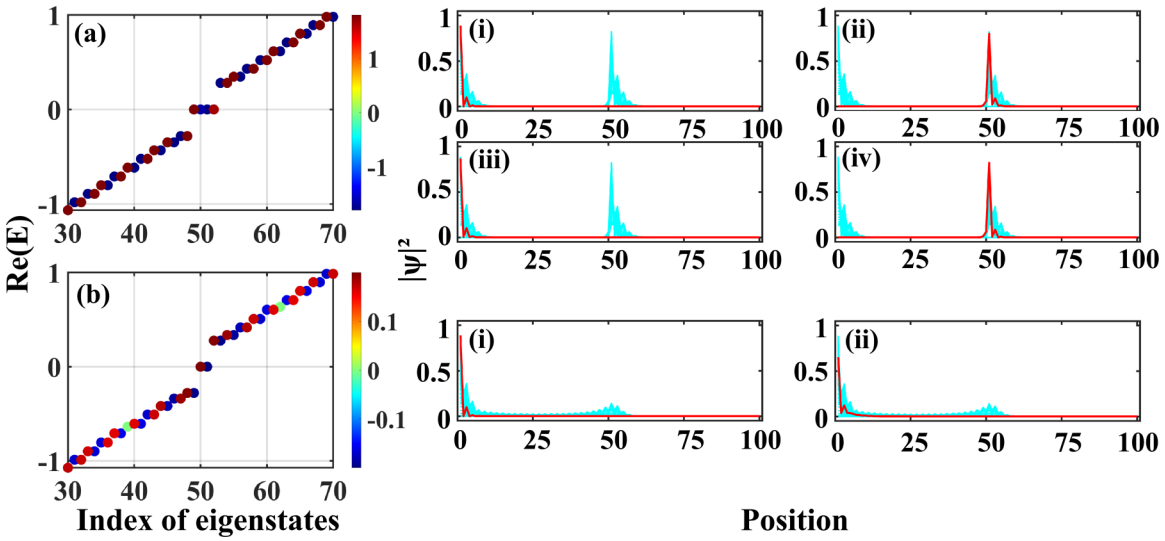

FIG. 10. Index of eigenstates and DOS selected from (a) phase region I ($t_1 = 1.0$, $\epsilon = 1.8$) and (b) phase region II ($t_1 = 1.0$, $\epsilon = 0.2$). The eigenvalues of edge states are [(a)(i)–(a)(iv)] $E = 1.8000i$, $-1.8000i$, $1.6720i$, and $-1.6720i$ and [(b)(i), (b)(ii)] $E = 0.2000i$ and $-0.2000i$.

potentials are manifested as $+i\epsilon$ on the right sides (LP $>$ 0) and $-i\epsilon$ on the left sides (LP $<$ 0). Thus, according to Table I, the positive-imaginary energy edge states of $E = X$ are localized on the left (LP $>$ 0) and negative-imaginary energy edge states are localized on the right (LP $<$ 0). For the case of $E \neq X$, the directions of edge states are based on the NHSE, so the localizations are on the left. In Fig. 11, we plot the DOS of the system with U_1'. It can be clearly observed that our inferred results by Sec. III are consistent with the figures.

For the case of $t_1 = 1.0$ at U_2', $t_1 = 1.666$ and $t_r = 0.334$, so the system satisfies $t_l > t_2 > |t_r|$. Based on the conclusions regarding $\mathbb{C}_1$ and $\mathbb{C}_3$, the system displays four parts of left-direction boundary NHSE at the left boundaries $j = 1$, the 1/4 position $j = 26$, 1/2 position $j = 51$, and 3/4 position $j = 76$ since there are three BPs. For the edge states, when the edge states belong to $E = X$, according to Table I, the localization directions of edge states are mainly adjusted by NHSE. When the edge states satisfy $E \neq X$ and large $|E - X|$, the directions of them are also adjusted by the LP (BP). In Fig. 11(b), we present the DOS results of different edge states for the situation of U_2', and we find that the localization property is indeed accordant with the conclusion in Sec. III.

Based on the above results, we can claim that the conclusions in Sec. III are correct and effective ways to predict the localization properties of edge states and bulk states.

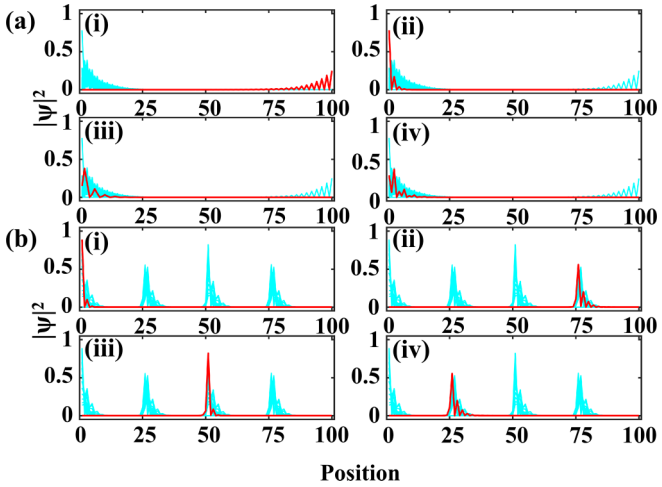

FIG. 11. (a) The DOS of edge states of $\epsilon = 0.9$ at $t_1 = 0.2$ in U_1' where (i) $E = 0.9000i$, (ii) $E = -0.900i$, (iii) $E = 0.4836i$, and (iv) $E = -0.4836i$. (b) The DOS of edge states of $\epsilon = 1.8$ at $t_1 = 1.0$ in U_2' where (i) $E = 1.7999i$, (ii) $E = -1.7999i$, (iii) $E = 1.6719i$, and (iv) $E = -1.6719i$.

V. CONCLUSION

In conclusion, in this paper we have performed a comprehensive analysis on the skin effects and topological properties in the nonreciprocal non-Hermitian SSH chain, by taking into account the presence of $\mathcal{PT}$-symmetric imaginary potentials. Following a detailed demonstration of the theoretical method, we have found that the application manners of the $\mathcal{PT}$-symmetric imaginary potentials play nontrivial roles in modulating the topological properties and the skin effect. When the $\mathcal{PT}$-symmetric imaginary potentials are applied to the two sites of each cell, the topological properties can be modulated obviously, with little change of the skin effect. On the other hand, if such potentials are applied according to two ending sites, the edge states will have complex localization. In the case of two domains of the SSH chain, both the topological properties and the skin effect can be modified in more independent manners. Therefore, the findings in this paper promote understanding of the influences of the interplay between the imaginary potentials and nonreciprocal couplings on the skin effects and topological properties in the SSH lattices.

ACKNOWLEDGMENTS

This work was financially supported by the LiaoNing Revitalization Talents Program (Grant No. XLYC1907033), the Natural Science Foundation of Liaoning province (Grants No. 2023-MS-072 and No. 2023-MSLH-218), the National Natural Science Foundation of China (Grant No. 11905027), Fundamental Research Funds for the Central Universities of Ministry of Education of China (Grants No. N2209005 and No. N2205015).

[1] C. M. Bender, D. C. Brody, and H. F. Jones, Complex extension of quantum mechanics, Phys. Rev. Lett. **89**, 270401 (2002).

[2] V. V. Konotop, J. Yang, and D. A. Zezyulin, Nonlinear waves in $\mathcal{PT}$-symmetric systems, Rev. Mod. Phys. **88**, 035002 (2016).

[3] Y. Ashida, Z. Gong, and M. Ueda, Non-Hermitian physics, Adv. Phys. **69**, 249 (2020).

[4] S. K. Özdemir, S. Rotter, F. Nori, and L. Yang, Parity-time symmetry and exceptional points in photonics, Nat. Mater. **18**, 783 (2019).

[5] C. Wu, N. Liu, G. Chen, and S. Jia, Non-Hermiticity-induced topological transitions in long-range Su-Schrieffer-Heeger models, Phys. Rev. A **106**, 012211 (2022).

[6] J. C. Budich and E. J. Bergholtz, Non-Hermitian topological sensors, Phys. Rev. Lett. **125**, 180403 (2020).

[7] F. Koch and J. C. Budich, Quantum non-Hermitian topological sensors, Phys. Rev. Res. **4**, 013113 (2022).

[8] A. McDonald and A. A. Clerk, Exponentially-enhanced quantum sensing with non-Hermitian lattice dynamics, Nat. Commun. **11**, 5382 (2020).

[9] M. Parto, S. Wittek, H. Hodaei, G. Harari *et al.*, Edge-mode lasing in 1D topological active arrays, Phys. Rev. Lett. **120**, 113901 (2018).

[10] S. Weidemann, M. Kremer, T. Helbig, T. Hofmann *et al.*, Topological funneling of light, Science **368**, 311 (2020).

[11] S. Garmon and K. Noba, Reservoir-assisted symmetry breaking and coalesced zero-energy modes in an open $\mathcal{PT}$-symmetric Su-Schrieffer-Heeger model, Phys. Rev. A **104**, 062215 (2021).

[12] J.-R. Li, L.-L. Zhang, W.-B. Cui, and W.-J. Gong, Topological properties in non-Hermitian tetratomic Su-Schrieffer-Heeger lattices, Phys. Rev. Res. **4**, 023009 (2022).

[13] A. Yoshida, Y. Otaki, R. Otaki, and T. Fukui, Edge states, corner states, and flat bands in a two-dimensional $\mathcal{PT}$-symmetric system, Phys. Rev. B **100**, 125125 (2019).

[14] A. F. Tzortzakakis, A. Katsaris, N. E. Palaiodimopoulos, P. A. Kalozoumis, G. Theocharis, F. K. Diakonos, and D. Petrosyan, Topological edge states of the $\mathcal{PT}$-symmetric Su-Schrieffer-Heeger model: An effective two-state description, Phys. Rev. A **106**, 023513 (2022).

[15] X. Zhu, H. Wang, S. K. Gupta, H. Zhang, B. Xie, M. Lu, and Y. Chen, Photonic non-Hermitian skin effect and non-Bloch bulk-boundary correspondence, Phys. Rev. Res. **2**, 013280 (2020).

[16] K. Xu, X. Zhang, K. Luo, R. Yu, D. Li, and H. Zhang, Coexistence of topological edge states and skin effects in the non-Hermitian Su-Schrieffer-Heeger model with long-range nonreciprocal hopping in topoelectric realizations, Phys. Rev. B **103**, 125411 (2021).

[17] S. M. Rafi-Ul-Islam, B. S. Zhuo, S. Haydar, C. H. Lee, and M. B. A. Jalil, Critical hybridization of skin modes in coupled non-Hermitian chains, Phys. Rev. Res. **4**, 013243 (2022).

[18] C. M. Bender and S. Boettcher, Real spectra in non-Hermitian Hamiltonians having $\mathcal{PT}$-symmetry, Phys. Rev. Lett. **80**, 5243 (1998).

[19] C. M. Bender, Making sense of non-Hermitian Hamiltonians, Rep. Prog. Phys. **70**, 947 (2007).

[20] L. Feng, R. El-Ganainy, and L. Ge, Non-Hermitian photonics based on parity-time symmetry, Nat. Photon. **11**, 752 (2017).

[21] A. Regensburger, C. Bersch, M. A. Miri, G. Onishchukov, D. N. Christodoulides, and U. Peschel, Parity-time synthetic photonic lattices, Nature (London) **488**, 167 (2012).

[22] Y. Wu, B. Zhu, S. F. Hu *et al.*, Floquet control of the gain and loss in a *PT*-symmetric optical coupler, Front. Phys. **12**, 121102 (2017).

[23] A. Stegmaier, S. Imhof, T. Helbig, T. Hofmann, C. H. Lee, M. Kremer, A. Fritzsche, T. Feichtner, S. Klembt, S. Hofling, I. Boettcher, I. C. Fulga, L. Ma, O. G. Schmidt, M. Greiter, T. Kiessling, A. Szameit, and R. Thomale, Topological defect engineering and $\mathcal{PT}$ symmetry in non-Hermitian electrical circuits, Phys. Rev. Lett. **126**, 215302 (2021).

[24] Z. Lin, J. Schindler, F. M. Ellis, and T. Kottos, Experimental observation of the dual behavior of $\mathcal{PT}$-symmetric scattering, Phys. Rev. A **85**, 050101(R) (2012).

[25] L. Lu, J. D. Joannopoulos, and M. Soljačić, Topological photonics, Nat. Photon. **8**, 821 (2014).

[26] M. G. Silveirinha, Topological theory of non-Hermitian photonic systems, Phys. Rev. B **99**, 125155 (2019).

[27] T. Ozawa, H. M. Price, A. Amo, N. Goldman, M. Hafezi, L. Lu, M. C. Rechtsman, D. Schuster, J. Simon, O. Zilberberg, and I. Carusotto, Topological photonics, Rev. Mod. Phys. **91**, 015006 (2019).

[28] L. Jin, P. Wang, and Z. Song, Su-Schrieffer-Heeger chain with one pair of $\mathcal{PT}$-symmetric defects, Sci. Rep. **7**, 5903 (2017).

[29] Y. Xing, L. Qi, J. Cao, D. Y. Wang, C. H. Bai, H. F. Wang, A. D. Zhu, and S. Zhang, Spontaneous $\mathcal{PT}$-symmetry breaking in non-Hermitian coupled-cavity array, Phys. Rev. A **96**, 043810 (2017).

[30] X. S. Li, Z. Z. Li, L. L. Zhang, and W. J. Gong, PT symmetry of the Su-Schrieffer-Heeger model with imaginary boundary potentials and next-nearest-neighboring coupling, J. Phys.: Condens. Matter **32**, 165401 (2020).

[31] K. Kawabata, Y. Ashida, H. Katsura, and M. Ueda, Parity-time-symmetric topological superconductor, Phys. Rev. B **98**, 085116 (2018).

[32] L. Jin, Topological phases and edge states in a non-Hermitian trimerized optical lattice, Phys. Rev. A **96**, 032103 (2017).

[33] L. L. Zhang, J. R. Li, D. Zhang, T. T. Xu, W. B. Cui, and W. J. Gong, $\mathcal{PT}$-symmetric non-Hermitian zigzag-edged ribbon of bilayer photonic graphene, Results Phys. **34**, 105274 (2022).

[34] X. M. Zhao, C. X. Guo, S. P. Kou, L. Zhuang, and W. M. Liu, Defective Majorana zero modes in a non-Hermitian Kitaev chain, Phys. Rev. B **104**, 205131 (2021).

[35] C. Yuce and H. Ramezani, Topological states in a non-Hermitian two-dimensional Su-Schrieffer-Heeger model, Phys. Rev. A **100**, 032102 (2019).

[36] S. Yao and Z. Wang, Edge states and topological invariants of non-Hermitian systems, Phys. Rev. Lett. **121**, 086803 (2018).

[37] S. Yao, F. Song, and Z. Wang, Non-Hermitian Chern bands, Phys. Rev. Lett. **121**, 136802 (2018).

[38] V. M. Martinez Alvarez, J. E. Barrios Vargas, and L. E. F. Foa Torres, Non-Hermitian robust edge states in one dimension: Anomalous localization and eigenspace condensation at exceptional points, Phys. Rev. B **97**, 121401(R) (2018).

[39] C. H. Lee and R. Thomale, Anatomy of skin modes and topology in non-Hermitian systems, Phys. Rev. B **99**, 201103(R) (2019).

[40] Y. Xiong, Why does bulk boundary correspondence fail in some non-Hermitian topological models, J. Phys. Commun. **2**, 035043 (2018).

[41] T. S. Deng and W. Yi, Non-Bloch topological invariants in a non-Hermitian domain wall system, Phys. Rev. B **100**, 035102 (2019).

[42] F. Song, S. Yao, and Z. Wang, Non-Hermitian topological invariants in real space, Phys. Rev. Lett. **123**, 246801 (2019).

[43] K. Yokomizo and S. Murakami, Non-Bloch band theory of non-Hermitian systems, Phys. Rev. Lett. **123**, 066404 (2019).

[44] E. Edvardsson, F. K. Kunst, T. Yoshida, and E. J. Bergholtz, Phase transitions and generalized biorthogonal polarization in non-Hermitian systems, Phys. Rev. Res. **2**, 043046 (2020).

[45] S. Masuda and M. Nakamura, Relationship between the electronic polarization and the winding number in non-Hermitian systems, J. Phys. Soc. Jpn. **91**, 043701 (2022); **91**, 114705 (2022).

[46] L. Xiao, T. S. Deng, K. K. Wang, G. Y. Zhu, Z. Wang, W. Yi, and P. Xue, Observation of non-Hermitian bulk-boundary correspondence in quantum dynamics, Nat. Phys. **16**, 761 (2020).

[47] P. C. Cao, Y. G. Peng, Y. Li, and X. F. Zhu, Phase-locking diffusive skin effect, Chin. Phys. Lett. **39**, 057801 (2022).

[48] A. Ghatak, M. Brandenbourger, J. van Wezel, and C. Coulais, Observation of non-Hermitian topology and its bulk-edge correspondence in an active mechanical metamaterial, Proc. Natl. Acad. Sci. USA **117**, 29561 (2020).

[49] E. J. Bergholtz, J. C. Budich, and F. K. Kunst, Exceptional topology of non-Hermitian systems, Rev. Mod. Phys. **93**, 015005 (2021).

[50] T. Helbig, T. Hofmann, S. Imhof, M. Abdelghany, T. Kiessling, L. W. Molenkamp, C. H. Lee, A. Szameit, M. Greiter, and R. Thomale, Chiral voltage propagation and calibration in a topolectrical Chern circuit, Nat. Phys. **16**, 747 (2020).

[51] L. Xiao, T. Deng, K. Wang, Z. Wang, W. Yi, and P. Xue, Observation of non-bloch parity-time symmetry and exceptional points, Phys. Rev. Lett. **126**, 230402 (2021).

[52] Y. Hu, F. Song, and Z. Wang, Generalized Brillouin zone and non-Hermitian band theory, Acta Phys. Sin. **70**, 230307 (2021).

[53] J. R. Li, C. Jiang, H. Su, D. Qi, L. L. Zhang, and W. J. Gong, Parity-dependent skin effects and topological properties in the multilayer nonreciprocal SuSchriefferHeeger structures, Front. Phys. **19**, 33204 (2024).